

Reynolds stresses transport in a turbulent channel flow subjected to streamwise traveling waves

Mohammad Umair * and Sedat Tardu 

University of Grenoble Alpes, CNRS, Grenoble-INP, LEGI, F-38000 Grenoble, France

Olivier Doche 

University of Grenoble Alpes, CNRS, Grenoble-INP, SIMAP, F-38000 Grenoble, France



(Received 17 January 2022; accepted 18 April 2022; published 6 May 2022)

Reynolds stresses transport in a turbulent channel flow under streamwise traveling waves is analyzed in detail using direct numerical simulations to gain physical insights into the mechanism of drag reduction. Streamwise traveling waves are known to produce larger drag reduction margins compared to simple homogeneous wall oscillations. The aim of the current investigation is to identify and analyze the direct effects arising from streamwise traveling waves that leads to larger drag reduction margins compared to simple homogeneous wall oscillations. Several cases were considered, with amplitudes ranging from 0.15 to 1.25 (in outer units) at fixed angular frequency and wave number of 0.16 and 1.66 (in outer units), respectively, to yield drag reduction margins ranging from 26% to 58%, respectively. Streamwise traveling waves of large amplitudes were found to block the intercomponent energy transfer, resulting in shut off of the near-wall buffer layer dynamics. The analyses here suggest that the combined effect of loss of communication between low and high buffer layers with damping in the wall-normal Reynolds stress component is associated to the traveling wave effect and results in larger drag reduction margins.

DOI: [10.1103/PhysRevFluids.7.054601](https://doi.org/10.1103/PhysRevFluids.7.054601)

I. INTRODUCTION

The demand to reduce energy consumption and control pollutants emissions has led researchers to devise various flow control techniques directed at reducing skin-friction drag. In a flow field, most of the skin-friction is generated in a thin highly viscous region close to the wall where the flow is highly turbulent. Skin-friction contributes to about 50% of the total drag in flow over a commercial aircraft [1] and almost 100% in internal flows (for example, parallel pipe and channel flows). It means that most of the energy used to drive the flow is dissipated by the wall due to skin-friction. Hence, a small reduction in skin-friction drag would result in substantial fuel savings.

Over several decades, various drag reduction (DR) techniques have been proposed. Based on whether the energy is fed into the system, DR techniques are classified as passive and active. Many passive DR techniques have been investigated in the past and shown to bring about sustained DR. However, due to their limited performance, active DR techniques have attracted considerable attention. Examples of passive DR techniques include the use of super-hydrophobic surfaces [2,3], riblets [4], etc. Compared to passive DR techniques, active DR techniques achieve larger DR margins under a wider range of flow conditions and operate at much larger spatio-temporal scales. Examples of active DR techniques include transverse wall oscillations [5], wall blowing and suction [6], rotating discs [7], plasma actuation [8], spanwise wall jet forcing [9], etc. Active DR

*mohammad.umair@legi.grenoble-inp.fr

techniques can be further classified into two categories, closed-loop techniques which require a feedback control law and open-loop techniques for which the control law is predetermined, and the control is applied independent of the instantaneous turbulent flow field, thus obviating the need for complex sensing and actuating systems.

Among many open-loop active DR techniques, one of the most promising candidates for reducing skin-friction drag is the transverse wall oscillations. Since introduced by Jung *et al.* [10], there have been a plethora of investigations, both experimental and numerical, devoted to quantify DR margins for a wide range of actuation parameters at low to moderate Reynolds number (Re). Numerous investigations, both numerical and experimental, have shown that the transverse wall oscillations in the form of streamwise traveling waves (STW) can produce significant DR margins as large as 60% and a net power savings of up to 26% can be achieved upon a careful selection of actuation parameters [11–15].

While considerable attention has been devoted in the past to the parametric studies, investigations that primarily aim at elucidating the mechanism behind drag reduction are rare. A few studies [10,16–26] exist that attempt to shed a light on the mechanism for a limiting case of a control where the spanwise wall oscillations are imposed homogeneously throughout the streamwise direction. Studies, for example of Jung *et al.* [10], Laadhari *et al.* [16], Choi *et al.* [17], Ricco [19], Toubert and Leschzner [21], etc., suggest that the forcing in the form of homogeneous wall oscillations results in the damping of the near-wall streaks strength, thickening of viscous sublayer, an upward shift in the logarithmic portion of the mean flow profile, a significant reduction in the sweep and ejection events associated with huge damping in the wall-normal turbulence intensity, etc. Xu and Huang [20] examined the transient response of a turbulent channel flow subjected to homogeneous spanwise wall oscillations for the first two oscillation periods. They found that the attenuation of pressure-strain correlations resulting in the hindrance of intercomponent transfer of turbulent kinetic energy is responsible for drag reduction. Toubert and Leschzner [21] showed that the cross-flow straining due to wall oscillations cause major distortions in the near-wall streaks strength which leads to a significant damping of wall-normal momentum exchange in the viscous sublayer and hence results in the suppression of wall-shear stress production. Yakeno *et al.* [23] studied the impact of wall oscillations on the structures of quasi streamwise vortices (QSVs) and found that the damping of ejection events governs the DR at relatively small oscillation periods. Ricco *et al.* [22], using direct numerical simulations at constant pressure gradient, carried out energy and enstrophy balances to emphasize the role of the oscillating spanwise shear layer and showed that drag reduction is associated with the increased dissipation rate of turbulent kinetic energy. Agostini *et al.* [24], on the other hand, found that the forcing in the form of wall oscillations results in a decrease in the turbulent dissipation rate at constant flow rate conditions.

While considerable advances have been made to unravel the physics of DR for simple homogeneous wall oscillations control, however, to this date, no advancement has been made to reveal the physical insights in the flows controlled by STW. The focus of most of the previous investigations, both experimental [15,27,28] and numerical [11–14], on STW control has been to find a scaling parameter that dictates DR margin. Some studies report at least some statistical information, for example, of Quadrio *et al.* [11] and Quadrio and Ricco [29], but the analyses are limited to the response of Reynolds stresses for very limited actuation scenarios. The objective of the present work is, therefore, to gain further insight into the physical mechanism behind STW control by analyzing and identifying the important interactions occurring within the budgets of Reynolds stresses. As we will see later in the discussions, some extra terms that are directly linked to the forcing appear in the transport equations of Reynolds stresses. These terms account for the interaction between the Reynolds stresses and the gradients of the periodic fluctuations due to forcing, and play a fundamental role in modifying the response of the Reynolds stresses, especially of the spanwise component. The approach is to identify the key terms appearing in the Reynolds stresses transport equations that are directly linked to the forcing. One of the secondary aims is also to investigate why STW control perform better than simple homogeneous wall oscillations.

TABLE I. %DR margins and the net power savings (% P_{net}) for different oscillatory conditions. The values of angular frequency (ω^*) and wave number (κ^*) of STW were kept fixed at 0.16 and 1.66 (outer units). Their corresponding values in local units are also provided to facilitate comparison with the available literature.

Case	A^* (U_c)	A_0 ($u_{\tau 0}$)	A (u_τ)	ω (u_τ^2/ν)	κ (u_τ/ν)	Re_τ (hu_τ/ν)	%DR	% P_{net}
HWO	0.51	12.0	14.9	0.098	—	144.2	36	-44
A0.15	0.15	3.5	4.0	0.027	0.248	156.9	26	23
A0.30	0.30	7.0	9.0	0.035	0.360	139.0	42	30
A0.50	0.50	11.7	16.1	0.039	0.408	130.7	48	15
A0.75	0.75	17.5	25.3	0.043	0.450	124.5	52	-19
A0.95	0.95	22.2	32.7	0.045	0.470	121.9	54	-50
A1.25	1.25	29.2	44.3	0.048	0.498	118.4	58	-130

The paper is divided into two main parts. Section II is devoted to the flow configuration and short details on the direct numerical simulations we used. The results (Sec. III) contains the Reynolds stress transport phenomena under STW, wherein the structural modifications observed in the near-wall turbulence are discussed in some details. Finally, the concluding remarks are provided in Sec. IV.

II. DETAILS OF FLOW CONFIGURATION AND NUMERICAL PROCEDURES

The configuration selected here is a fully developed incompressible channel flow. The Reynolds number $\text{Re} = hU_c/\nu$ was fixed at 4200, where U_c is the centerline velocity of the Poiseuille flow, h is the channel half-width, and ν is the kinematic viscosity. For the uncontrolled case, it corresponds to friction Reynolds number $\text{Re}_{\tau 0} = hu_{\tau 0}/\nu = 180$, where $u_{\tau 0}$ is the friction velocity of the uncontrolled flow. The flow is subjected to spanwise wall oscillations in the form of STW, which is prescribed by

$$W^*(x^*, y^* = 0, z^*) = A^* \sin(\kappa^* x^* - \omega^* t^*), \quad (1)$$

where W^* is the instantaneous spanwise velocity, A^* is its amplitude at the wall, κ^* is the wave number in the streamwise direction, and ω^* is the angular frequency of the traveling wave. Here x^* , y^* , z^* represent the streamwise, wall-normal, spanwise directions, respectively, and t^* is time. The superscript $*$ denotes quantities normalized using outer units; absence of this qualifier implies scaling in inner units. The values of ω^* and κ^* were kept fixed at 0.16 and 1.66, respectively, while the amplitude was varied from $A^* = 0.15$ to 1.25. The corresponding %DR margins are listed in Table I. The chosen set of ω^* and κ^* corresponds to the optimal settings at $A^* = 0.50$ and leads to $DR = 48\%$, which is in good agreement with Quadrio *et al.* [11]. Concerning the net power savings (% P_{net}), it is well known that there is a penalty in imposing wall actuation control. The net power saving is computed in the same manner as described in Quadrio *et al.* [11] and are provided in Table I. The estimated % P_{net} compare well with these authors. It is important to note that the large imposed amplitude A0.95 case results in roughly the same net power saving as the simple homogeneous wall oscillations (HWO) case; however, the drag reduction margin is significantly larger. This strengthens the main aim of this investigation, namely, looking for the physical process that makes the STWs more efficient. The range of actuation parameters considered here has been narrowed down to the optimum case scenario to investigate the direct effect of STW on the near-wall turbulence dynamics. The naming of the cases is based on the forcing amplitude in outer units, for example, the case A1.25 refers to the STW controlled case of imposed amplitude $A^* = 1.25$. One of the aims here is to investigate the direct effects of the STW with respect to the simple homogeneous wall oscillations (HWO). Transverse wall oscillations in the form of STW result in larger DR margin compared to HWO. We will show and discuss in detail later that some terms

appearing in the Reynolds stresses transport equations are a direct consequence of the STW. The response of the flow to the STW is rather complex when examined as a function of ω^* and κ^* . Depending on the value of κ^* , drag can be either increased or decreased for a fixed value of ω^* . Therefore, it is difficult to compare both types of forcing on the basis of actuation parameters. Yet, a clear base has to be defined for comparison; hence, we opted to compare the traveling wave effects with the HWO in their optimal configuration with $A_0 = 12$ ($A^* = 0.51$) and $T_0 = 100$ for the Re investigated here [21,30]. Note that the optimal configuration is a function of Re [13,14]. Here, the subscript ‘0’ represents quantities scaled by the friction velocity of the uncontrolled flow.

Direct numerical simulations (DNS) were performed using MULTIFAST, a highly parallel code developed by our team that solves incompressible Navier-Stokes equations using explicit optimized (EO) finite difference schemes for spatial discretization and low-storage third-order Runge-Kutta method to advance the solution in time. MULTIFAST has been used previously in many studies [31–34]. Further details about the numerical scheme is provided in Appendix A.

All simulations were performed over the same computational box of size $L_x = 6\pi h$, $L_y = 2h$, $L_z = 3\pi h$ in the streamwise, wall-normal, and spanwise direction, respectively. The box was covered by $N_x \times N_y \times N_z = 401 \times 129 \times 335$ (≈ 17.3 million) nodes, which were distributed uniformly along the streamwise and spanwise directions, while they were clustered in the wall-normal direction near the wall through a hyperbolic tangent distribution. The corresponding cell dimensions were $\Delta x_0, \Delta y_0, \Delta z_0 = 8.5, 0.5-5.5, 5$. The simulation for the uncontrolled flow was performed at a constant time-step $dt_0 = 0.04$, which is well below that used in previous studies at larger Re [12,14,21,24,35]. The statistics for the uncontrolled flow were obtained using a total of 50 snapshots covering a time window of $t_0 \approx 37\,000$, separated by $\Delta t_0 \approx 770$.

Two different inner scaling options are available in the constant flow rate (CFR) conditions for the controlled cases, one based on the inner variables derived using the friction velocity of the uncontrolled flow ($u_{\tau 0}$) and the other based on the inner variables derived using the respective local (actual) friction velocities of the controlled cases (u_τ). As the flow is still in turbulent regime even at the largest imposed amplitude, the use of actual friction velocity of the controlled flow is physically correct, especially near the wall. Moreover, since the imposed control is based on the wall and its influence is limited to the near-wall region, the use of actual friction velocity would bring about the important structural changes in the flow field. Scaling with the inner variables based on $u_{\tau 0}$ brings about the absolute changes of the quantities, while scaling with the local inner variables based on u_τ leads to the direct *in situ* nondimensionalization of the mean flow near the wall, and thus allows for a comparison between the near-wall drag-reduced statistics and the statistics of the uncontrolled flow at the same friction Reynolds number (Re_τ) [21,22]. Real structural changes can only be analyzed through local units; this point will be further illustrated in the later sections.

Throughout the manuscript, the quantities with subscript ‘0’ are normalized using the inner variables based on $u_{\tau 0}$; absence of this qualifier implies scaling with inner variables based on u_τ of the controlled cases.

Considering the periodic nature of the imposed control, the fluctuations associated with the wall forcing must be removed to obtain the purely stochastic fluctuations. Hence, for statistical analyses we adopt the classical triple decomposition introduced by Hussain and Reynolds [36] to decompose an instantaneous flow field variable (F) into a time-invariant mean component (\overline{F}), a periodic fluctuating component (\tilde{F}), arising due to the periodic forcing, and a purely stochastic component (f), characterizing the turbulent fluctuations. The decomposition can be expressed as

$$F = \overline{F} + \tilde{F} + f = \langle F \rangle + f, \quad (2)$$

where $\langle F \rangle$ is the phase-averaged value of F . This convention is followed throughout the manuscript. The flow field variables were phase-averaged over the phase $\xi = x - ct$ of the traveling wave, where $c = \omega/\kappa$ is the speed of the traveling wave. Figures 1(a) and 1(b) show the phasewise variations of the phase-averaged spanwise velocity at different wall-normal locations for A0.50 case.

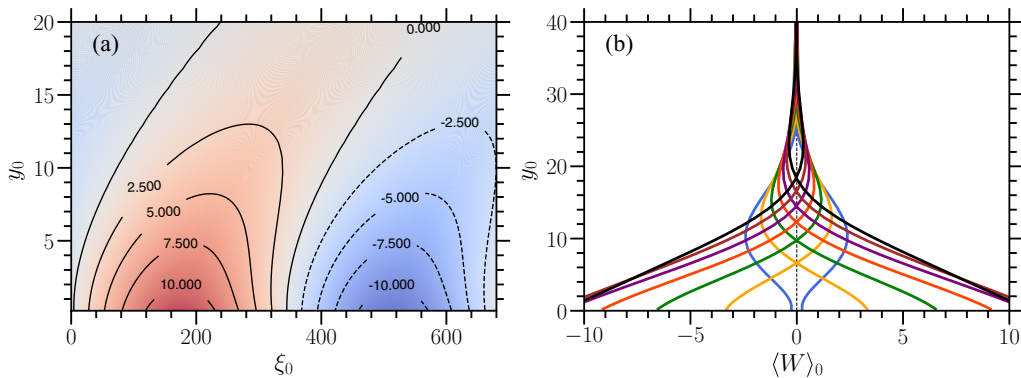


FIG. 1. Phasewise variations of phase-averaged spanwise velocity $\langle W \rangle_0$ at different wall-normal locations y_0 for A0.50 case. The red contours in the left figure correspond to positive values, while the blue contours correspond to negative values.

For the controlled cases, the uncontrolled flow was used as the initial condition, and the time-step was reduced to $dt_0 = 0.008$ to converge the phase-averaged statistics. At least 20 initial cycles were discarded to ensure that the time window over which the data was collected to perform statistics doesn't overlap with the transient phase over which the control leads the flow towards the drag reduced state. To ensure the convergence of the phase-averaged statistics, the data was collected for at least 40 cycles corresponding to a time window of $t_0 \approx 12000$. The details about the convergence of the phase-averaged statistics is provided in Appendix B. All the simulations were performed on the computational clusters of GRICAD, University of Grenoble-Alpes. Even at such a low Re, each simulation for the controlled case typically required CPU-time of about 90 000 core-hours, distributed across 128 processors.

III. RESULTS AND DISCUSSIONS

A. Skin-friction coefficient and the mean flow

The skin-friction coefficient (C_f) is defined as

$$C_f = \frac{2\tau_w}{\rho U_b^2}, \quad (3)$$

where U_b is the bulk flow velocity, ρ is the density of the fluid, and τ_w is the shear stress at the wall. The %DR margin is quantified in terms of relative change in C_f ,

$$\%DR = (1 - C_f/C_{f0}) \times 100, \quad (4)$$

where C_{f0} is the skin-friction coefficient of the uncontrolled flow.

Figure 2(a) shows the initial response of C_f (normalized by C_{f0}) after the actuation of control. C_f began to decrease sharply, and the rate of the initial decay is similar for all forcing amplitudes, except for A0.15 case. The response of the large amplitude cases are quite interesting, for instance, the flow is not far from the relaminarization limit at $A^* = 1.25$ near $t_0 = 2000$ but returns back to a turbulent state at $t_0 = 3000$. Such complex responses of skin-friction are also observed in optimal wall turbulence control at moderate optimization horizons (see Fig. 11 of Bewley *et al.* [37]).

The time of initial decay varies with the amplitude of forcing and is about 5–6 cycles ($t_0 \approx 1600$) for A0.15 case, and 13–14 cycles ($t_0 \approx 4000$) for A1.25 case. After the elapsed of the initial transient phase, the flow acquires a new quasistationary state, and C_f begins to oscillate about a mean level. The period of oscillation of C_f differs with the amplitude of forcing, but in general it is about one order of magnitude longer than the period of forcing.

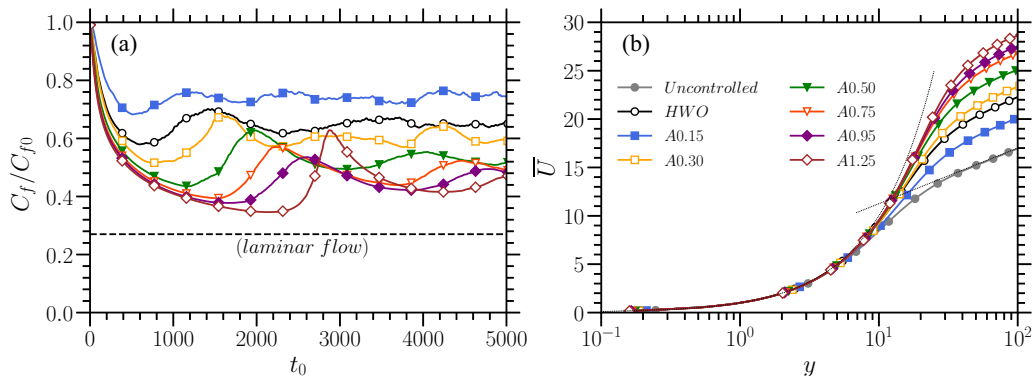


FIG. 2. (a) Initial response of the normalized skin friction coefficient (C_f/C_{f0}) after the actuation of control for different forcing amplitudes. (b) Mean velocity profiles for the uncontrolled and controlled cases.

Figure 2(b) conveys the effect of forcing on the mean velocity profile. Consistent with the previous studies, the mean velocity profiles show an upward shift in the logarithmic portion and thickening of the viscous sublayer when scaled with the respective friction velocities of the drag reduced flows. This behavior is typical to drag reduction scenarios regardless of the control type—except for superhydrophobic surfaces, where drag reduction results in thinning of the buffer layer along with a downward shift in the logarithmic region. The magnitude of the upward shift in the logarithmic portion is proportional to the DR margin [14].

B. Reynolds stresses components

Figure 3 shows the effect of forcing on the Reynolds stresses components for the uncontrolled and controlled cases. Forcing results in a substantial decline in the streamwise component \overline{uu} [Fig. 3(a)], especially close to the wall, reflecting a strong reduction in the near-wall streaks strength. The peak value of \overline{uu} is shifted away from the wall and reflects the lifting of the quasistreamwise vortices (QSVs) [38]. An interesting feature worth noticing is that the profiles of \overline{uu} approximately collapse for $y > 30$, reflecting that the structural changes brought up by the control are limited to the region close to the wall. The peak value of the wall-normal component \overline{vv} progressively declines as the amplitude of the forcing is increased [see Fig. 3(c)]. Contrary to \overline{uu} , the location of its peak remains unaffected. It is important to stress that \overline{vv} plays the primary role in the production of Reynolds shear stress \overline{uv} . Attenuation of \overline{vv} indicates damping of sweep and ejection events that are primarily responsible for most of the turbulent kinetic energy production. Likewise, the magnitude of \overline{uv} also shows a substantial decline at all wall-normal locations [Fig. 3(c)] with a significant reduction close to the wall.

The response of the spanwise component \overline{ww} is strikingly different, with the emergence of a second peak at $y \approx 8$ near the edge of the viscous sublayer at the largest imposed amplitude $A^* = 1.25$ investigated here [see Fig. 3(b)]. Despite the appearance of two production terms arising in its transport equation due to forcing (see Appendix C), \overline{ww} progressively declines at wall-normal locations $y > 20$. It is important to note that these peculiar behaviors can hardly be detected if the quantities were scaled with the friction velocity of the uncontrolled flow. To stress this point, we show in Fig. 3(d) the profiles of \overline{ww}_0 , where the scaling is now with respect to the friction velocity of the uncontrolled flow ($u_{\tau 0}$). It is clearly seen that the peculiar structural modifications are hardly discernible in Fig. 3(d) in comparison to Fig. 3(b). Scaling with local inner variables results in correct nondimensionalization and allows sorting out the structural changes of the response of the near-wall turbulence.

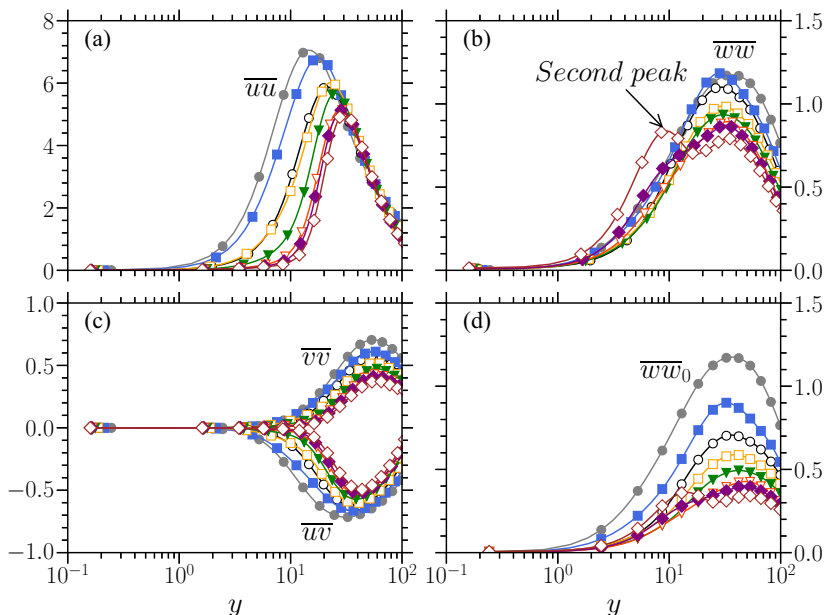


FIG. 3. Reynolds stresses profiles for uncontrolled and controlled cases. (a) streamwise component \overline{uu} , (b) spanwise component \overline{ww} (scaled with local friction velocity), (c) wall-normal component \overline{vv} and Reynolds shear stress \overline{uv} , and (d) spanwise component \overline{ww}_0 (scaled with the friction velocity of the uncontrolled flow). The profiles in panels (a), (b), and (c) were scaled with the local friction velocity, while the profiles in panel (d) were scaled with the friction velocity of the uncontrolled flow. Refer to Fig. 2 for markers corresponding to different cases.

To summarize, globally, the profiles of Reynolds stresses components approximately collapse for $A^* \geq 0.75$ when scaled with the local friction velocity, except the spanwise component \overline{ww} . The streamwise component \overline{uu} is significantly damped close to the wall, reflecting a strong reduction in the near-wall streaks strength. The peaks of \overline{uu} and \overline{uv} shifts toward the edge of the buffer layer at $y \approx 30$ [see Figs. 3(a) and 3(c)]. The profile of spanwise component \overline{ww} for the A1.25 case exhibits a second peak close to the wall at $y \approx 8$; this unique feature is explained in the following section. Discarding the appearance of the second peak in \overline{ww} at $A^* = 1.25$, the wall-normal locations of the peak values of \overline{vv} and \overline{ww} are not altered by the STW. Again, all these quantities were scaled using the local friction velocity. When scaled with the friction velocity of the uncontrolled flow, all the peak values are shifted away from the wall in proportion to $u_{\tau 0}/u_{\tau} = \sqrt{1/(1-DR)}$.

C. Mean Reynolds stresses budgets

The Reynolds stresses transport equations for the streamwise component \overline{uu} , wall-normal component \overline{vv} , spanwise component \overline{ww} , and shear stress \overline{uv} are provided in Appendix C. Besides the classical terms, quantities directly related to the STW emerge in the transport equations. These extra terms account for the interaction between the phase-averaged Reynolds stresses and the gradients of the periodic fluctuations due to forcing. All the extra terms emerging from the wall-normal and streamwise gradients of $\langle U_i \rangle$ (where $i = 1, 2, 3$ denote streamwise, wall-normal, and spanwise direction, respectively) are negligible compared to the other terms in the overall budget of Reynolds stresses components, except for those intervening in the spanwise component \overline{ww} induced by $\partial \langle W \rangle / \partial x$ and $\partial \langle W \rangle / \partial y$, as shown in Fig. 4. Recall that, the production term in the transport equation of \overline{ww} is zero for the canonical (uncontrolled) channel flow. Hence, the level of \overline{ww} is maintained solely by the velocity-pressure gradient term $\overline{\Pi_{ww}} = -2w \partial p / \partial z$, the role of which is to

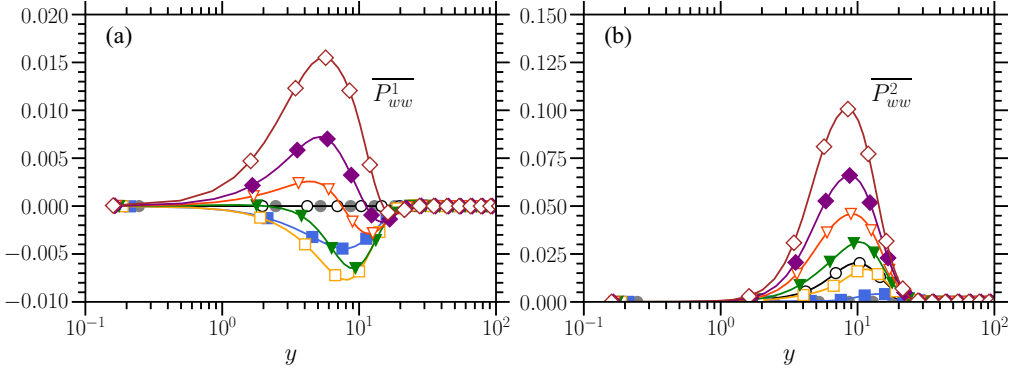


FIG. 4. Extra production terms (a) $\overline{P_{ww}^1} = -2\overline{\langle wu \rangle} \partial \tilde{W} / \partial x$ and (b) $\overline{P_{ww}^2} = -2\overline{\langle wv \rangle} \partial \tilde{W} / \partial y$ appearing in the transport equation of spanwise Reynolds shear stress component $\overline{w\overline{w}}$. Refer to Fig. 2 for markers corresponding to different cases.

extract energy from \overline{uu} and transfer it to $\overline{w\overline{w}}$. However, under the presence of STW, two production terms coming from the streamwise and wall-normal gradients of $\langle W \rangle$ emerge in the transport equation of $\overline{w\overline{w}}$. These terms are denoted by $\overline{P_{ww}^1} = -2\overline{\langle wu \rangle} \partial \tilde{W} / \partial x$ and $\overline{P_{ww}^2} = -2\overline{\langle wv \rangle} \partial \tilde{W} / \partial y$, respectively, in Appendix C. Curiously enough, the total production $\overline{P_{ww}} = \overline{P_{ww}^1} + \overline{P_{ww}^2}$ increases in the low buffer layer, with a maximum at $y \approx 8$ for cases with amplitudes $A^* > 0.50$, as seen in Fig. 5(e). This explains the emergence of the second peak in $\overline{w\overline{w}}$ observed in Fig. 3(b) at the same wall-normal location.

The production term $\overline{P_{ww}^1}$ is negative for small imposed amplitudes $A^* \leq 0.50$ [see Fig. 4(a)], but $\overline{P_{ww}^2}$, which is strictly positive at all wall-normal locations [see Fig. 4(b)], largely overcomes the total mean production $\overline{P_{ww}}$ in the viscous and low buffer layers. Both, $\overline{\langle P_{ww}^1 \rangle}$ and $\overline{\langle P_{ww}^2 \rangle}$ are strongly modulated and reach very large values during the ξ -cycle. These peculiar behaviors will be further elucidated in the Sec. III D, where we discuss the phasewise variations of transport quantities. At this stage, it is important to point out, in particular, the response of the velocity-pressure gradient correlations $\overline{\Pi_{uu}}$ and $\overline{\Pi_{ww}}$, shown in Figs. 5(b) and 5(f), respectively. It is seen that the increase in $\overline{P_{ww}}$ [see Fig. 5(e)] is accompanied by a strong decrease in the velocity-pressure gradient term $\overline{\Pi_{ww}}$. The latter is entirely annihilated within the low buffer and viscous sublayers $y < 8$ when the imposed amplitude is beyond $A^* > 0.5$ [see Fig. 5(f)]. Remark that, in the uncontrolled channel flow $\overline{\Pi_{ww}}$ is large in the buffer layer with a maximum at $y \approx 10$, as the velocity-pressure gradient term is the main source term in the transport equation of $\overline{w\overline{w}}$. In canonical wall-bounded turbulent flows, the intercomponent transfer $\overline{uu} \rightarrow \overline{w\overline{w}}$ is established through the velocity-pressure gradient correlations $\overline{\Pi_{uu}} \rightarrow \overline{\Pi_{ww}}$. This process fades away next to the wall up to the top of the low buffer layer in the presence of STW of large enough amplitudes $A^* > 0.5$. Indeed, $\overline{\Pi_{uu}}$ progressively goes to zero as amplitude increases in concordance with $\overline{\Pi_{ww}}$ [see Figs. 5(b) and 5(f)]. Thus, interestingly enough, the communication between \overline{uu} and $\overline{w\overline{w}}$ is cut off at $y < 8$, and as a consequence the spanwise turbulent intensity $\overline{w\overline{w}}$ evolves somewhat freely, with a local equilibrium between the production and dissipation $\overline{P_{ww}} \approx -\overline{\epsilon_{ww}}$, in a rough sense [see Fig. 5(e)], with the slight differences being compensated by the turbulent transport $\overline{T_{ww}}$ and viscous diffusion $\overline{D_{ww}}$ (not shown).

Unlike $\overline{w\overline{w}}$, the net production term $\overline{P_{vv}}$ in the transport equation of the wall-normal component $\overline{v\overline{v}}$ is zero in the flows altered by STW. Hence, it is fair to state that the mechanism responsible for maintaining the level of $\overline{v\overline{v}}$ is similar to that for the uncontrolled case, i.e., intercomponent energy transfer $\overline{uu} \rightarrow \overline{v\overline{v}}$ through $\overline{\Pi_{uu}} \rightarrow \overline{\Pi_{vv}}$. Similar to what was observed for $\overline{w\overline{w}}$ transport, the communication $\overline{uu} \rightarrow \overline{v\overline{v}}$ fades away in the low buffer layer as $\overline{\Pi_{vv}} \sim \overline{\Pi_{uu}} \approx 0$ for large imposed amplitudes of STW, resulting in a strong decline in $\overline{v\overline{v}}$ close to the wall, as seen in Fig. 3(c).

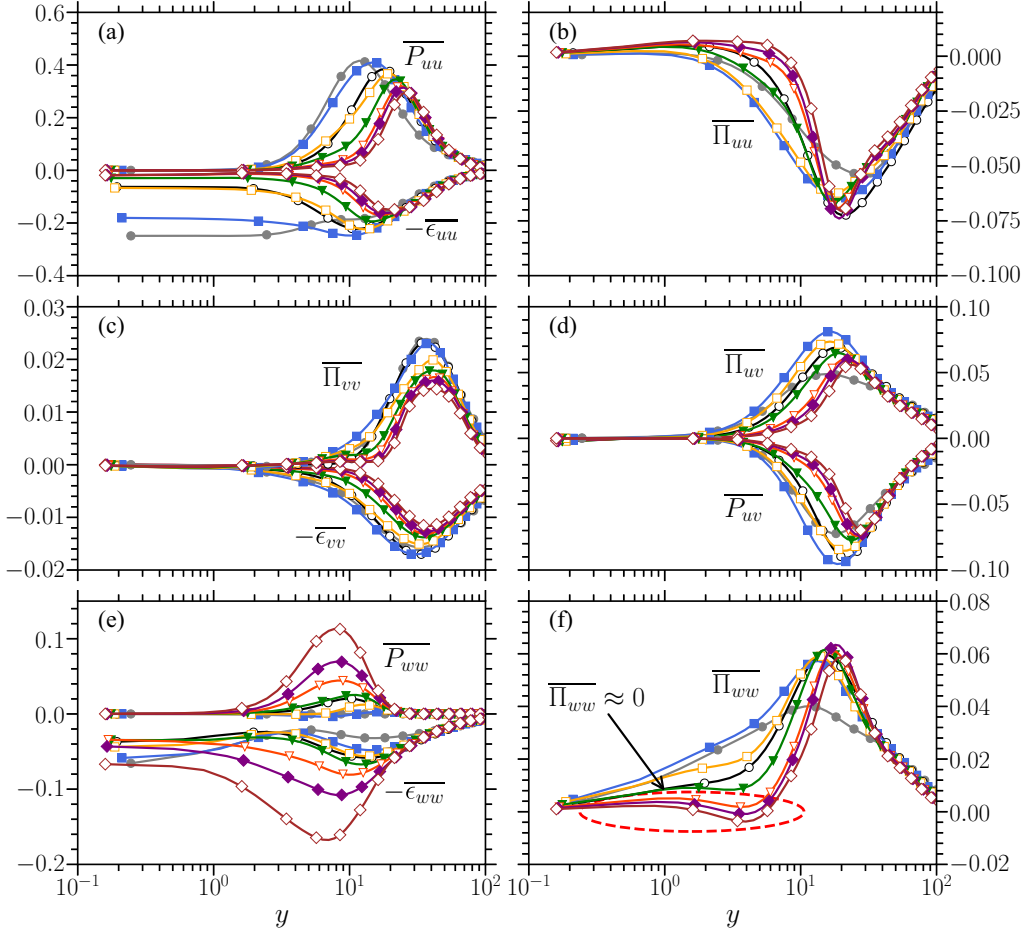


FIG. 5. Wall-normal distributions of terms appearing in the transport equations of Reynolds stresses components. (a) Production $\overline{P_{uu}}$, dissipation $-\overline{\epsilon_{uu}}$; (b) velocity-pressure gradient $\overline{\Pi_{uu}}$ term for streamwise component \overline{uu} ; (c) velocity-pressure gradient $\overline{\Pi_{vv}}$, dissipation $-\overline{\epsilon_{vv}}$ term for wall-normal component \overline{vv} ; (d) velocity-pressure gradient $\overline{\Pi_{uv}}$, production $\overline{P_{uv}}$ term for shear stress component \overline{uv} ; (e) production $\overline{P_{ww}}$, dissipation $-\overline{\epsilon_{ww}}$; and (f) velocity-pressure gradient $\overline{\Pi_{ww}}$ term for spanwise component \overline{ww} . Refer to Fig. 2 for markers corresponding to different cases.

Overall, as seen in Fig. 5(c), the budget of \overline{vv} is dominated by the velocity-pressure gradient $\overline{\Pi_{vv}}$ and dissipation $\overline{\epsilon_{vv}}$. Globally, the profiles of $\overline{\Pi_{vv}}$ and $\overline{\epsilon_{vv}}$ approximately collapse for large imposed amplitudes $A^* > 0.50$ of the STW. As the production of shear stress $\overline{P_{uv}}$ is directly linked to \overline{vv} , such a collapse is expected. It is pertinent to stress here again that these peculiar behaviors arise upon scaling with the local inner variables. The response of the \overline{vv} transport to STW is quite similar to that observed in the simple homogeneous wall oscillations control [21].

The transport of Reynolds shear stress \overline{uv} is dominated by the production $\overline{P_{uv}}$ and the velocity-pressure gradient $\overline{\Pi_{uv}}$ terms [see Fig. 5(d)]. The role of $\overline{\Pi_{uv}}$ is to reduce the magnitude of \overline{uv} . As forcing results in a strong decline in \overline{vv} , consequently, $\overline{P_{uv}}$ drops drastically at large imposed amplitudes of STW. Correspondingly, $\overline{\Pi_{uv}}$ declines, and the slight difference is absorbed by a relatively low turbulent diffusion $\overline{D_{uv}}$ and viscous diffusion $\overline{D_{uv}^v}$ (not shown). The profiles of $\overline{P_{uv}}$ and $\overline{\Pi_{uv}}$ collapse very well for the cases with amplitudes $A^* \geq 0.75$.

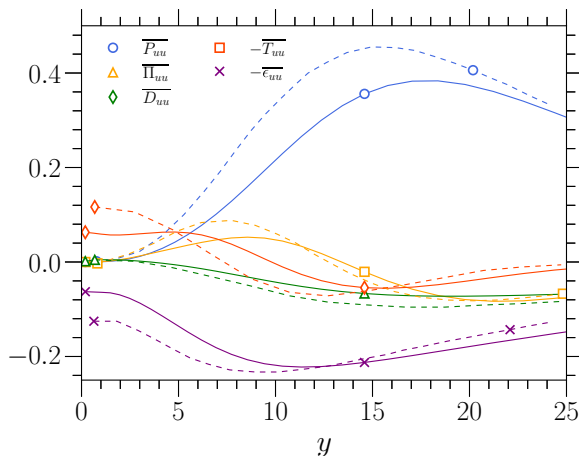


FIG. 6. Comparison of transport terms in the \overline{uu} budget for HWO case (solid lines) with Touber and Leschziner [21] data (broken lines) at $Re_\tau = 500$ at same control parameters.

One of the aims of this investigation is to sort out the proper effects of the imposed STW that result in larger DR margins compared to HWO. The interpretation would be straightforward if we could detect direct effects arising from $\partial \langle U_i \rangle / \partial x$ in the transport terms, but unfortunately that was not the case. Consequently, we decided to compare the traveling wave effects with the HWO in their optimal configuration with $A_0 = 12$ ($A^* = 0.51$) and $T_0 = 100$, for reasons stated earlier. Globally, the ensemble of the transport terms corresponding to HWO fall between $A^* = 0.15$ and $A^* = 0.50$ cases of the STW. There is some noticeable decrease of $\overline{\Pi_{ww}}$ in the buffer layer in the HWO case too [Fig. 5(b)]. This particular point has already been nicely discussed in Touber and Leschziner [21]. However, in the entire low buffer layer $\overline{\Pi_{ww}}$ annihilation is clearly a real effect of large amplitude STW and this is quite uncommon in wall turbulence control. Note, by the way that, the suppression of $\overline{\Pi_{ww}}$ points at the entire decorrelation between the pressure and spanwise local gradient $\partial w / \partial z$, since $\overline{\Pi_{ww}} = -2\rho \overline{\partial w / \partial z}$ by spanwise homogeneity. Furthermore, the transport terms in the HWO case compare globally well with the distributions of Touber and Leschziner [21], at the same oscillation parameters but larger Re_τ . Figure 6 compares the \overline{uu} transport terms in HWO obtained here and those of Touber and Leschziner [21] at $Re_\tau = 500$, next to the wall. It is seen that the distributions collapse qualitatively well. In the absence of more objective criteria, it would be, therefore, fair to attribute the structural modifications observed here at $A^* > 0.50$ to the effect of STW itself. The structural modification brought up by the STW are discussed later in Sec. III E. Here, we briefly discuss the response of turbulent streamwise vorticity ω_x to highlight the structural modifications. Detailed results on the vorticity transport mechanism under STW will be reported separately.

The velocity-pressure gradient term $\overline{\Pi_{ww}}$ next to the wall can be related to the flux of ω_x . This has not been noticed before to our best knowledge. Indeed, in the region very close to the wall in the viscous sublayer, the spanwise turbulent intensity can be related to the streamwise turbulent vorticity by $w \approx y\omega_{x,0}$. Here, the subscript “0” refers to the wall. Furthermore, the pressure gradient $\partial p / \partial z$ at the wall is equal to the flux of ω_x , i.e., $\partial p / \partial z|_{y=0} = \partial \omega_x / \partial y|_{y=0}$. Combining gives the near-wall asymptotic behavior,

$$\overline{\Pi_{ww}} = -2 \overline{\left\langle w \frac{\partial p}{\partial z} \right\rangle} \approx -y \frac{\partial \langle \omega_x^2 \rangle}{\partial y} \Big|_{y=0}. \quad (5)$$

Figure 7(a) shows the wall-normal distribution of $\overline{\omega_x^2}$. Equation (5) predicts in an excellent manner the near-wall behavior of $\overline{\Pi_{ww}}$ in the canonical flow [Fig. 5(f)]. The wall gradient $\partial \overline{\Pi_{ww}} / \partial y|_0$

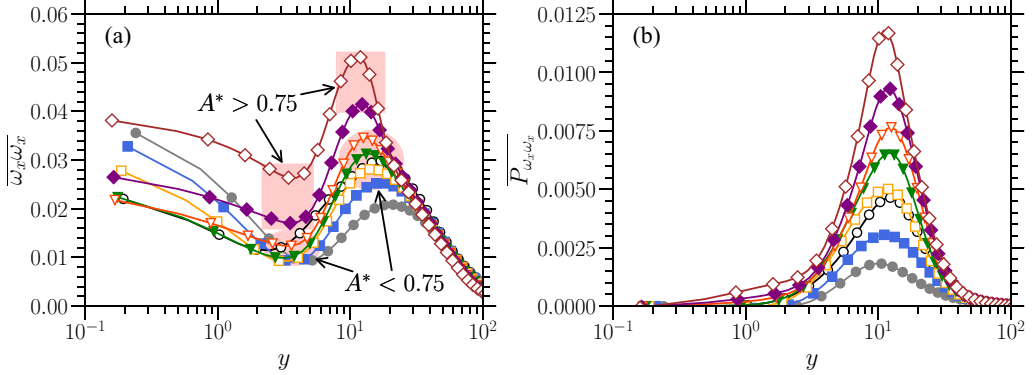


FIG. 7. Wall-normal distribution of (a) the streamwise component of turbulent enstrophy $\overline{\omega_x \omega_x}$ and (b) its production term. Note in the above figure that the local maxima and minima emanating from different cases are relatively well regrouped for $A^* < 0.75$ including HWO. The profiles gradually deviate once $A^* > 0.75$, pointing at severe alterations of the near-wall coherent eddies regeneration process. Refer to Fig. 2 for markers corresponding to different cases.

is 0.01 in Fig. 5(f) and coincides perfectly with $-\partial \langle \overline{\omega_x^2} \rangle / \partial y_{y,0}$ in Fig. 7(a) for the uncontrolled case. The lack of correlation $\overline{\Pi_{ww}} \approx 0$ in the flows altered by STW of large amplitudes would imply $\langle \overline{\omega_x^2} \rangle \approx \text{constant}$ next to the wall according to Eq. (5). There is indeed a significant undermining of $\overline{\omega_x^2}$ variations in the viscous sublayer once $A^* > 0.50$. For instance, at $A^* = 1.25$, $\overline{\omega_x^2}$ varies only by 20% from the wall to its local minimum at $y = 3.5$. This variation is an order of magnitude smaller than that in the uncontrolled flow, in which $\overline{\omega_x^2}$ decreases by 400% from the wall to its local minimum at $y = 5$.

The occurrence of a local minimum and maximum in $\overline{\omega_x^2}$ is attributed to the QSVs [39]. The local maxima $\overline{\omega_{x,\text{max}}^2}$ is the intensity of the QSVs, and the local minima is the consequence of the no-slip boundary condition. The Rankine vortex model introduced by Kim *et al.* [39] estimate acceptably well the streamwise turbulent vorticity at the wall induced by QSVs through $\overline{\omega_{x,0}^2} = (9/4)\overline{\omega_{x,\text{max}}^2}$ in the canonical wall-bounded flows. This crude model predicts acceptably well $\overline{\omega_{x,0}^2}$ for the smallest amplitude $A^* = 0.15$, but fails at larger amplitudes. This is either because the model is too crude, and/or there are important structural changes in the flow field because of the presence of STW. Note in Fig. 7 that the local maxima and minima emanating from different cases are relatively well regrouped for $A^* < 0.75$ including HWO. However, once $A^* > 0.75$ the profiles gradually deviate, pointing at severe alterations of the near-wall coherent eddies regeneration process.

To summarize, the communication in the intercomponent transfer is cut off by the traveling waves of $A^* > 0.50$ in the low buffer layer, in which $\overline{\Pi_{uu}} \sim \overline{\Pi_{ww}} \approx 0$. The low and high buffer layers are disconnected. The consequence is the push-up of the peak of the shear stress production $\overline{P_{uw}}$ from $y = 15$ in the uncontrolled flow to $y = 30$ at $A^* > 0.50$ [see Fig. 5(d)]. The shift in the peak of \overline{uw} to $y = 30$ results in the shift of the \overline{uu} production $\overline{P_{uu}}$ to the same wall-normal location Fig. 3(a). The buffer layer dynamics which is capital in canonical wall-bounded turbulence is shut off. It is seen in Fig. 3(c) that there is a strong damping of the wall-normal turbulent activity, in agreement with earlier investigations [21]. The local maximum of $\overline{\Pi_{vv}}$ and $\overline{\epsilon_{vv}}$ decrease systematically with the increasing amplitudes, and the decrease is as large as 40%. The weakening in $\overline{\Pi_{vv0}}$ and $\overline{\epsilon_{vv0}}$, scaled by the inner variables based on the friction velocity of the uncontrolled flow, is as large as 70% at $A^* = 1.25$. Thus, the damping of the wall-normal activity still remains a key phenomenon under the presence of traveling waves. However, it is important to note that $\overline{\Pi_{vv}}$ and $\overline{\epsilon_{vv}}$ are well regrouped for all the cases investigated here, once they are properly scaled by the local inner variables. Since,

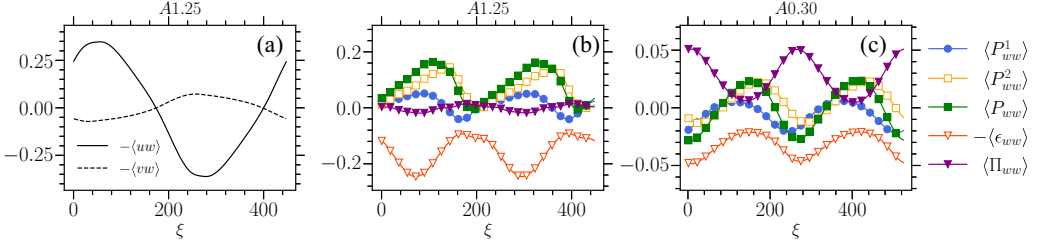


FIG. 8. (a) Phasewise variations of $-\langle uw \rangle$ and $-\langle vw \rangle$ at $y = 15$ for A1.25 case. Phasewise variations of $\langle P^1_{ww} \rangle$, $\langle P^2_{ww} \rangle$, $\langle P_{ww} \rangle$, $-\langle \epsilon_{ww} \rangle$, and $\langle \Pi_{ww} \rangle$ at $y = 5$ for (b) A1.25 and (c) A0.30 cases, respectively. Note how $\langle \Pi_{ww} \rangle$ for A1.25 case is entirely frozen compared to A0.30 case where there are large modulations.

the results related to HWO fall again within $0.15 < A^* < 0.50$, the combined effect of the loose of communication between the low and high buffer layers with the $\overline{v\overline{v}}$ damping is related to the traveling waves effect.

D. Phasewise variations of transport quantities

The phase averages of different terms emerging in the Reynolds stresses transport equations have been carefully determined and analyzed in detail. Globally, the cyclic variations of turbulent quantities are constrained at $y < 15$ where $\partial\langle W \rangle/\partial y$ is significant. The most salient effects are found in the terms related to $D\langle ww \rangle/Dt$ and will shortly be discussed hereafter.

The mean correlations \overline{uw} and \overline{vw} are zero, as in the case of uncontrolled flow (not shown). However, both of them, especially, $\langle uw \rangle$ reaches large cyclic variations up to the edge of the Stokes layer induced by the STW. Figure 8(a) shows $\langle uw \rangle$ and $\langle vw \rangle$ at $y = 15$ for A1.25 case. It can be seen that the cyclic variations in $\langle vw \rangle$ are smaller compared to $\langle uw \rangle$. Yet, the shear $\partial\langle W \rangle/\partial y$, which is proportional to A^* (for fixed ω^* and κ^*), reaches large cyclic values close to the wall at large imposed amplitudes. The consequence are the large cyclic modulations in $\langle P^1_{ww} \rangle$ and $\langle P^2_{ww} \rangle$. Figure 8(b) shows the cyclic variations of terms that significantly contributes to $\langle ww \rangle$ transport at $y = 5$ for A1.25 case. Note first that $\langle P^1_{ww} \rangle$ reaches negative values at some phases, thus becomes locally an annihilation term. Yet, $\langle P^2_{ww} \rangle$, which is larger and positive, overcomes $\langle P^1_{ww} \rangle$ so that $\langle P_{ww} \rangle > 0$. Second, the dissipation is not locally in equilibrium with the production, pointing to truly unsteady effects due to STW actuation. Finally, note in Fig. 8(b) that the velocity-pressure gradient correlation is entirely frozen during the whole cycle, i.e., $\langle \Pi_{ww} \rangle \approx 0$. The fact that the large amplitude traveling waves aborts the $uu \rightarrow ww$ communication can be better appreciated once Fig. 8(c) is compared with Fig. 8(b). The latter shows the phase averages of $\langle ww \rangle$ transport terms at the same wall-normal location $y = 5$, but at a lower imposed amplitude $A^* = 0.30$. It is clearly seen that the velocity-pressure gradient term $\langle \Pi_{ww} \rangle$ responds to the unsteady wave, and that its modulation amplitude is comparable to that of $\langle P_{ww} \rangle$. Note also in Fig. 8(c) that $\langle P^1_{ww} \rangle$ is negative almost throughout the whole cycle and destroys production $\langle P_{ww} \rangle$. The latter is even negative during half of the cycle. The response of $\langle ww \rangle$ changes strongly at large imposed amplitudes, wherein the DR is larger than HWO. Thus, it is reasonable to directly attribute the behavioral changes of the near-wall turbulence at $A^* > 0.50$ to the traveling waves.

E. Effects on streaks and shear layers

The low- and high-speed streaks of spanwise velocity are the signatures of the QSVs in the early periods of their regeneration process [40]. The w -streaks spacing is roughly 100 wall-units in the buffer layer, similar to the spanwise spacing of low- and high-speed streaks of streamwise velocity. Figure 9(b) shows the w -streaks in the uncontrolled flow at $y = 10$. The structural modification brought up by the STW of large amplitudes are clearly visible in Fig. 9(k). It can be seen that

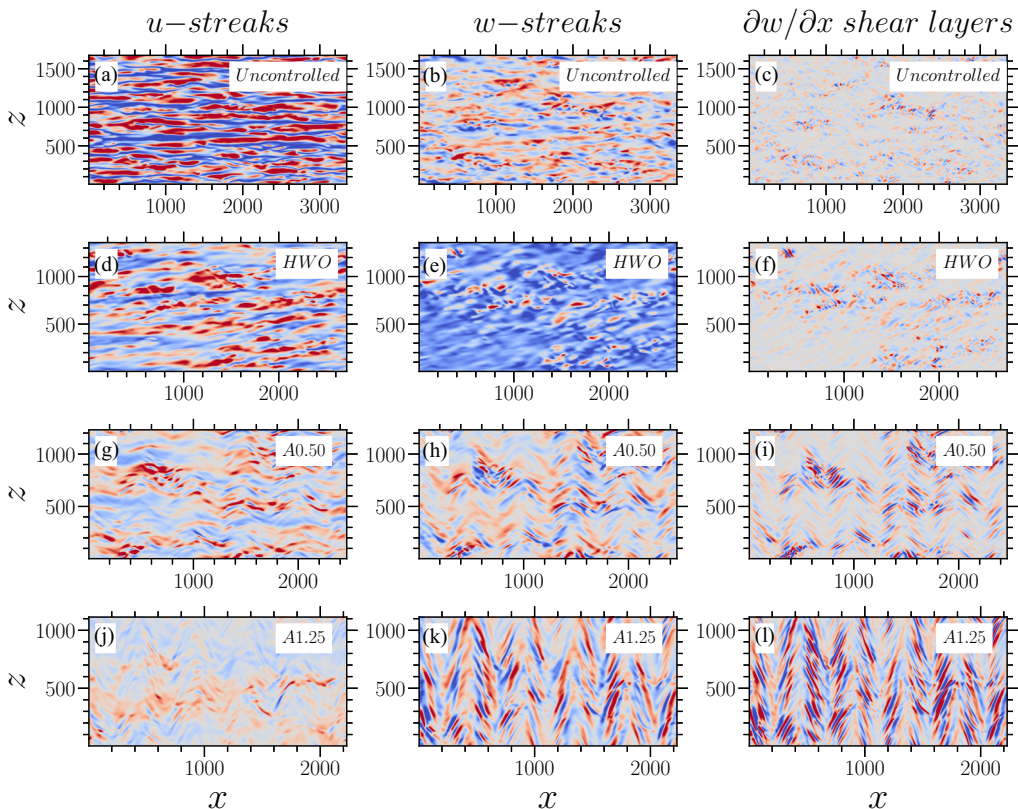


FIG. 9. Streamwise velocity fluctuations (u) at $y = 10$ for (a) uncontrolled, (d) HWO, (g) A0.50, and (j) A1.25 cases, respectively. The blue color represents the low-speed u -streaks ($u < 0$), while the red color represents the high-speed u -streaks ($u > 0$). The contours are in the range -3 to $+3$. Note that u was scaled by the local friction velocity; had it been scaled by the friction velocity of the uncontrolled flow, the streaky structures would have disappeared, especially for the large DR cases. Spanwise velocity fluctuations (w) at $y = 10$ for (b) uncontrolled, (e) HWO, (h) A0.50, and (k) A1.25 cases, respectively. The blue color represents the low-speed w -streaks ($w < 0$), while the red color represents the high-speed w -streaks ($w > 0$). The contours are in the range -2 to $+2$. Note that w was scaled by the local friction velocity. The instantaneous visualizations of the $\partial w / \partial x$ shear layers at $y = 10$ for (c) uncontrolled, (f) HWO, (i) A0.50, and (l) A1.25 cases, respectively. The blue color represents the negative, while the red color represents the positive values. The contours are in the range -0.1 to $+0.1$. Here also $\partial w / \partial x$ was scaled by the local friction velocity. Note that the heavily modulated Λ -shaped structures of $\partial w / \partial x$ start to appear for cases with large imposed amplitudes of STW. These structures are absent for both the uncontrolled and HWO cases.

the longitudinal w -streaks are tilted in the spanwise direction and are now organized in Λ -shaped patterns. This peculiar spanwise reorganization appears at amplitudes $A^* > 0.50$. A similar reorganization of the u -streaks [Fig. 9(j)] is also observed, even though the communication between u and w is cut off in the low buffer layer for the reasons stated earlier. The usual characteristics of the u - and w -streaky structures are recovered only at $y > 20$.

Both u - and w -streaky structures are the footprints of the QSVs that are mainly responsible for the production of Reynolds shear stress in the buffer layer in canonical wall-bounded flows. The individual self-organization of w in the low buffer layer has a direct consequence on the regeneration of the active QSVs. In the canonical wall layer, the main regeneration term of the local streamwise turbulent vorticity ω_x in the low buffer layer comes from the tilting of the wall-normal

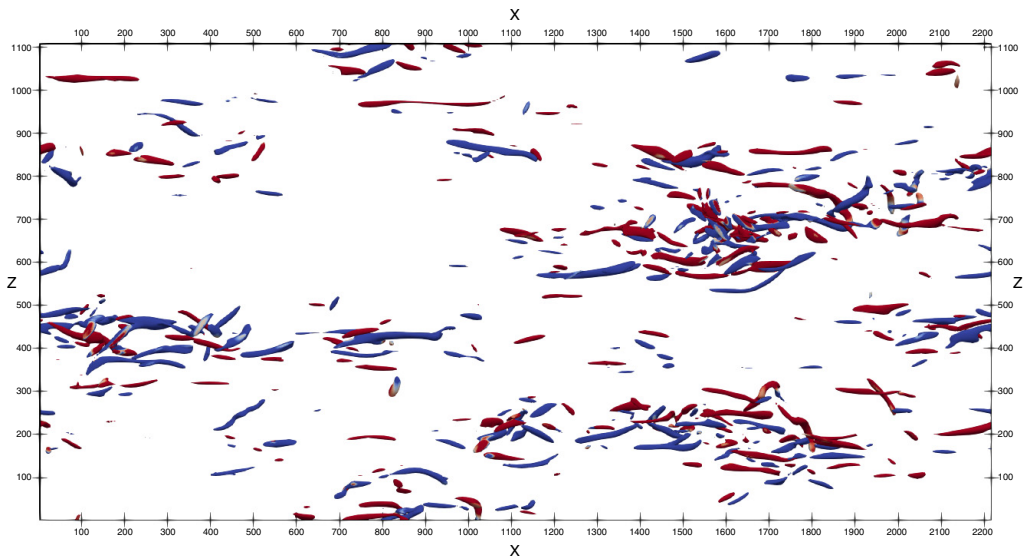


FIG. 10. (Top View) Instantaneous near-wall vortical structures ($\lambda_2 = -0.02$) scaled by the local inner variables for the A1.25 case. The regions where $\omega_x > 0$ are colored in red and where $\omega_x < 0$ are colored in blue.

turbulent vorticity ω_y and reduces to $-\frac{\partial w}{\partial x} \frac{\partial \bar{U}}{\partial y}$. Brooke and Hanratty [41] had shown that the tilting term overcomes twisting and stretching at $y < 10$ and peaks at $y = 8$. Like u - and w -streaks, the structures of the $\partial w/\partial x$ shear layers are strongly altered by the STW of large amplitudes. These shear layers [in Fig. 9(l)] are also organized in similar Λ -shaped patterns as observed for w -streaks in Fig. 9(k).

The main production term of the enstrophy transport $D\overline{\omega_x\omega_x}/Dt$ is still the term related to the tilting of the $\partial w/\partial x$ shear layers in the controlled flow. Figure 7(b) shows the production term $P_{\omega_x\omega_x} = -2\langle\omega_x\partial w/\partial x\rangle d\bar{U}/dy$. It is seen that $P_{\omega_x\omega_x}$ peaks at $y \approx 10$ and increases with the imposed amplitude A of the STW. Note in Fig. 7(b) that $P_{\omega_x\omega_x}$ is an order of magnitude larger at $A^* = 1.25$ than that in the uncontrolled flow. The HWO case coincides well with $A^* = 0.30$, strengthening again, that $A^* = 0.30$ is the lower limit above which the direct effect of STW are felt in the wall turbulence.

The Λ -shaped shear layers are organized as alternating positive $\partial w/\partial x > 0$ and $\partial w/\partial x < 0$ structures in Figs. 9(i) and 9(l). Their legs are inclined along the spanwise direction by roughly $\pm\pi/4$. They are tilted by the shear $d\bar{U}/dy \approx 1$ near $y = 10$ (not shown). The key question here is to determine whether these shear layers roll-up into coherent vortices or not. This is important since the coherent active eddies lead to the generation of the Reynolds shear stress uv and the drag. In case of roll-up, the resulting topological structure of the coherent structures near the wall would be seriously altered at large imposed amplitudes, by the apparition of contrarotating vortices strongly inclined along the spanwise direction coming from the unfamiliar topological nature of $\partial w/\partial x$. We carefully analyzed the λ_2 structures using tens of snapshots, in particular for the $0.75 < A^* < 1.25$ cases. The symmetric and antisymmetric parts of the velocity gradient tensor from which the second-largest eigenvalue is determined are conveniently scaled by the local inner variables. A movie is available for A1.25 case as a supplementary material online [42]. Figures 10 and 11 show the top and side views of an instantaneous snapshot of λ_2 structures for the A1.25 case. The structures with $\omega_x > 0$ are colored in red and $\omega_x < 0$ in blue. One finds the classical topological features of the QSVs observed in the uncontrolled flow. Thus, the peculiar $\partial w/\partial x$ layers tilted by the mean shear in Figs. 9(i) and 9(l) clearly do not roll-up into coherent vortices. The vast majority of the coherent

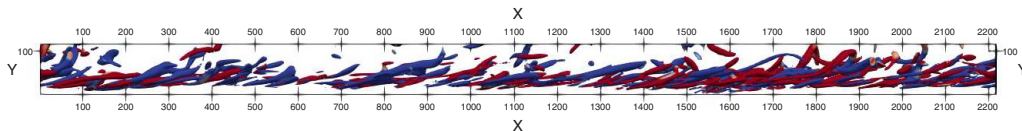


FIG. 11. (Side View) Instantaneous near-wall vortical structures ($\lambda_2 = -0.02$) scaled by the local inner variables for the A1.25 case. The regions where $\omega_x > 0$ are colored in red and where $\omega_x < 0$ are colored in blue.

structures reach their maturity well above $y = 20$ (Fig. 11). In Sec. III C, we discussed in detail the disconnection at large amplitudes of the Reynolds stresses transport between low and high buffer layers. The only remaining possibility of communication that remained was the generation of the coherent active eddies emanating from the roll-up of the atypical shear layers of Figs. 9(i) and 9(l). This possibility by now is also discarded.

Last but not least, it is noticeable that the QSVs are systematically organized as packets at $A^* > 0.75$ and have similarities with the transitional-turbulent spots [43]. Packets of vortices, or large-scale motions, containing typically three individual structures, exist in the uncontrolled flow, including at moderate Re [44,45]. At $A^* > 0.75$, on the one hand, the packets are comparatively more common, and on the other hand, they contain a much larger number of individual structures similar to turbulent spots.

IV. CONCLUDING REMARKS

Direct numerical simulations were performed to investigate the effect of transverse wall oscillations in the form of streamwise traveling waves on the Reynolds stresses transport, for the first time to our best knowledge. The angular frequency and the wavelength of the STW were fixed at $\omega^* = 0.16$ and $\kappa^* = 1.66$, and the imposed amplitude was varied nearly by one decade from $A^* = 0.15$ to $A^* = 1.25$. The drag reduction at the largest amplitude reaches 58%. The results were compared with homogeneous spanwise wall oscillations case with imposed period $T_0 = 100$ and amplitude $A_0 = 12$, to identify the proper impact of the STW on the near-wall turbulence.

Forcing in the form of the STW results in substantial decline of all the Reynolds stresses components. The transport terms are in close similarity with HWO when the imposed amplitude of the STW are within the intermediate range $0.30 < A^* < 0.50$. This regime is marked by a strong damping of the wall normal velocity fluctuations on one hand, and some noticeable decline in the velocity-pressure gradient correlations, on the other. The present investigation globally confirms previously published results on HWO.

The situation changes drastically in the large amplitude STW's cases when $A^* > 0.50$. The intercomponent transfer between the Reynolds stresses fade away in the low buffer layer, wherein it is found that $\overline{\Pi_{uu}} \sim \overline{\Pi_{vv}} \sim \overline{\Pi_{ww}} \approx 0$. The annihilation of $\overline{\Pi_{ww}}$ at $y < 10$ is particularly spectacular. It is shown that $\overline{\Pi_{ww}} \approx 0$ in the low buffer layer results in the flattening of the streamwise vorticity intensity near the wall and points at a strong alteration of the active eddies regeneration process. The spanwise component $\overline{w\tilde{w}}$ is autonomously produced by the Stokes strain related terms $P_{ww}^1 = -2\langle wu \rangle \partial \tilde{W} / \partial x$ and $P_{ww}^2 = -2\langle wv \rangle \partial \tilde{W} / \partial y$ in the low buffer layer, and the production simply dissipates. Unexpectedly large values of the phase averages $\langle wu \rangle$ are observed at $A^* > 0.75$, but P_{ww}^2 dominates the $\overline{w\tilde{w}}$ production in the low buffer layer as $\partial \tilde{W} / \partial y \gg \partial \tilde{W} / \partial x$.

The buffer layer streaky structures are also strongly altered at large A^* . The most spectacular modification takes place in the $\partial w / \partial x$ shear layers that become strongly inclined in the spanwise direction and alternates between positive and negative values quite coherently. The intensity in these shear layers is related to the major streamwise vorticity production in the low buffer layer, in the uncontrolled and as well as controlled flows. However, there is no topological signature of these shear layers in the active eddies' regeneration process. Thus, the peculiarly different $\partial w / \partial x$

shear layers do not roll-up in the low buffer layer. At $A^* > 0.75$, the quasistreamwise vortices are organized as packets of several vortices typical of transitional turbulent spots.

The low and high buffer layer get disconnected at large forcing amplitudes. Forcing also results in the cutoff of intercomponent energy transfer between different Reynolds stresses components. The low buffer layer becomes autonomous, self-sustained by pure Stokes strain effects. The capital role of the low buffer layer in the uncontrolled flow is by-passed by forcing, resulting in a disconnection with the high buffer layer. This situation is rather uncommon in the near-wall turbulence control.

ACKNOWLEDGMENTS

The simulations of the controlled cases were performed using the GRICAD infrastructure [46], which is supported by Grenoble research communities. The simulations of the uncontrolled case were performed using the Froggy platform of the GRICAD infrastructure [46], which is supported by the Région Auvergne-Rhône-Alpes (GRANT CPER07_13 CIRA) and the Agence Nationale de la Recherche (Equip@Meso project Reference No. ANR-10-EQPX-29-01 of the programme Investissements d'Avenir).

APPENDIX A: COMPUTATIONAL DETAILS

The Navier-Stokes equation scaled by the channel half width h and the centerline velocity U_c together with the continuity equation reads

$$\frac{\partial u_i}{\partial t} + \frac{\partial u_i u_j}{\partial x_j} = -\frac{\partial p}{\partial x_i} + \frac{1}{\text{Re}} \frac{\partial^2 u_i}{\partial x_j^2}, \quad \frac{\partial u_i}{\partial x_i} = 0, \quad (\text{A1})$$

where u_i is the i th velocity component, p is the pressure, and $\text{Re} = hU_c/\nu$ is the Reynolds number (ν being the kinematic viscosity). The computational domain is a rectangular box of size $L_x \times L_y \times L_z$, where L_x , L_y and L_z are the extents of the domain in the streamwise (x), wall-normal (y), and spanwise direction (z), respectively. The computational domain is discretized by a structured mesh using $N_x \times N_y \times N_z$ points. The boundary conditions are the no-slip at the wall and periodic in the streamwise and spanwise directions. The mesh points are uniformly along the streamwise and spanwise directions, while they are refined near the wall in the wall-normal direction through a hyperbolic tangent distribution.

Spatial numerical operators are expressed by using fifth-order explicit optimized (EO) finite differences scheme. EO schemes are derived from the dispersion-relation-preserving (DRP) schemes (see Bauer *et al.* [47] for technical details). In contrast to compact scheme discretization, an explicit scheme requires only the function value at the neighboring points to approximate the derivatives. Hence, the derivative estimations are direct while it necessarily implies a matrix inversion in the compact schemes.

Considering the temporal integration, the solution at the next time (sub)iteration $k + 1$ is explicitly obtained by integrating Eq. (A1). The time interval $[t, t + \Delta t]$ is divided into n_k substeps ($t_1 = t, t_2, t_3, \dots, t_{n_k} = t + \Delta t$). By applying the fractional step method, the velocity is corrected to become solenoidal at each time iteration. Making use of the conventional Einstein notation for spatial coordinate and velocity components (for which subscripts 1,2,3 refer, respectively, to the spanwise (x), wall-normal (y), and streamwise (z) component), the temporal advancement of Eq. (A1) can be expressed as

$$u^{k+1} = u^k + R_{\text{pmean}} + R_{\text{pfluc}} + R_{\text{adv}} + R_{\text{diff}}, \quad (\text{A2})$$

where

$$R_{\text{pmean}} = - \int_{t_k}^{t_{k+1}} \left(\overline{\frac{\partial p}{\partial x_i}} \right) dt, \quad R_{\text{pfluc}} = - \int_{t_k}^{t_{k+1}} \left(\frac{\partial p'}{\partial x_i} \right) dt,$$

$$R_{\text{adv}} = - \int_{t_k}^{t_{k+1}} \left(\frac{\partial u_i u_j}{\partial x_j} \right) dt, \quad R_{\text{diff}} = \frac{1}{\text{Re}} \int_{t_k}^{t_{k+1}} \left(\frac{\partial^2 u_i}{\partial x_j^2} \right) dt,$$

$(\partial \bar{p} / \partial x_i)$ and $(\partial p' / \partial x_i)$ stand for the mean and the fluctuating pressure gradient, respectively. R_{pmean} is evaluated through the global flow rate conservation. The advection (R_{adv}) and diffusion (R_{diff}) terms are estimated explicitly from the previous ($k - 1$) and the current (k) fields as

$$R_{\text{adv}} + R_{\text{diff}} = \alpha_k \Delta t \left(- \frac{\widehat{\partial u_i u_j}}{\partial x_j} + \frac{1}{\text{Re}} \frac{\widehat{\partial^2 u_i}}{\partial x_j^2} \right)_k + \beta_k \Delta t \left(- \frac{\widehat{\partial u_i u_j}}{\partial x_j} + \frac{1}{\text{Re}} \frac{\widehat{\partial^2 u_i}}{\partial x_j^2} \right)_{k-1}, \quad (\text{A3})$$

where $\widehat{(\cdot)}$ denotes spatially discretized operators.

The time advancement is performed by a Runge-Kutta third-order (RK3) scheme in which the coefficients involved in the three iteration steps are $\alpha_{1,2,3} = [8/15, 5/12, 3/4]$ and $\beta_{1,2,3} = [0, -17/60, -5/12]$. The quantity R_{pfluc} is evaluated from the pressure at $k + 1$. Equation (A3) can be reformulated as

$$u^{k+1} = \widetilde{u}^{k+1} - (\alpha_k + \beta_k) \Delta t \nabla \widehat{p}^{(k+1)}, \quad (\text{A4})$$

where $\widetilde{u}^{k+1} = u^k + R_{\text{pmean}} + R_{\text{adv}} + R_{\text{diff}}$ is the first estimation of the velocity field based on the terms known at the current time iteration. The quantity $p^{(k+1)}$ is then calculated by applying the divergence free operator to Eq. (A4), and solving the resulting Poisson equation:

$$\nabla^2 \widehat{p}^{(k+1)} = \frac{1}{\Delta t (\alpha_k + \beta_k)} \nabla \widetilde{u}^{k+1}. \quad (\text{A5})$$

The Poisson equation for the pressure is solved in the Fourier domain (through FFT decomposition) at each xz plane.

APPENDIX B: VALIDATION AND STATISTICAL CONVERGENCE

There are mainly three particularities of the present DNS: First, the resolution is very fine, with the mesh size in the wall-normal direction Δy being 1/3 of the Kolmogorov scale (η) near the wall while $\Delta y \approx 1.4\eta$ at the centerline. The resolution in the near wall region compares with previous DNS, but it is much finer in the core region here. The mesh size in the streamwise direction is as small as twice the Kolmogorov length at the centerline. The mesh size in the spanwise direction is about η at the centerline. The grid employed in the present study is sufficiently fine to resolve the relevant scales present in the turbulent flow field, and is even finer in the streamwise and spanwise directions compared with many other published DNS studies on channel flows. The second particularity of these DNS is the use of particularly large computational domains: the streamwise and spanwise lengths of the computational domain are $6\pi h$ and $3\pi h$. They are taken particularly large to accommodate multiple wavelengths. The third is the use of fifth-order explicit optimized (EO) finite differences scheme, which resulted in near spectral resolution. The adequacy of the resolution was examined by comparing the profiles of the root-mean-square velocity and vorticity components with the data of Moser and Kim [48] at $\text{Re}_\tau = 180$ in Fig. 12. (For the sake of brevity, Fig. 12 is not included in the manuscript.) As seen in Fig. 12, the profiles of root-mean-square velocity and vorticity components match perfectly with the data of Moser and Kim [48].

In the controlled flow, however, the determination of the stochastic field requires the introduction of the triple decomposition, defined as

$$F = \langle F \rangle + f, \quad (\text{B1})$$

where F is the instantaneous field, $\langle F \rangle$ is the phase-averaged field, and f is the purely stochastic field. The computation of phase-averaged field requires division of the wave cycle into bins of equal widths. We typically chose 200–500 bins, depending on the amplitude of the forcing. To improve the

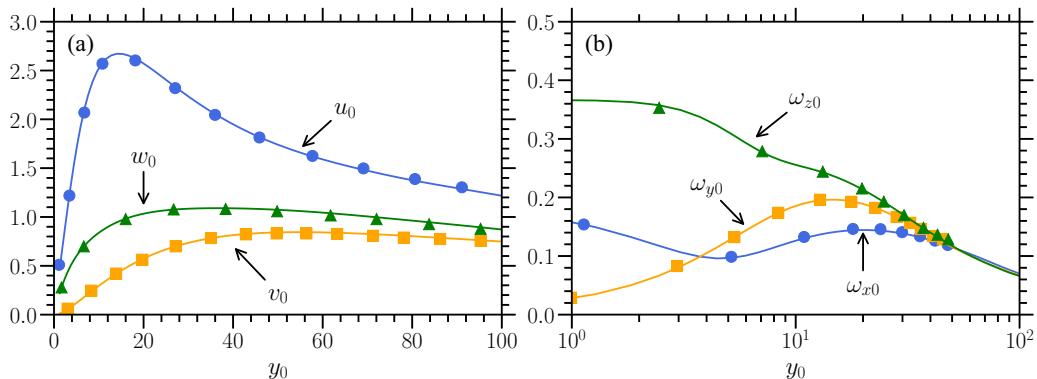


FIG. 12. Comparison of (a) root-mean-square velocity and (b) root-mean-square vorticity components in the streamwise, spanwise, and wall-normal directions with the data of Moser and Kim [47] (in markers).

convergence, we further decreased the time-step to increase the number of variables collected per bin. We tested the convergence of the phase-averaged statistics by computing the ensemble average of the quantities such as Reynolds stresses over 5, 10, 15, 20, etc., cycles. In view of the very high associated costs involved in running the simulation for very long durations, we decided to perform averages over 40 temporal cycles, which is yet very long compared to other studies at even larger Reynolds number. The conclusion that the errors are small is strengthened by the fact that tests with averaging over 20 cycles gave fields very close to those with averaging over all 40 cycles. Despite the fair smoothness observed for all the quantities, the phase-averaged quantities cannot be fully converged because of the presence of the large-scale oscillations in C_f . However, the error is small (less than 1.5%), as illustrated by Fig. 13. To avoid cluttering, only the error margins for the A1.25 case are shown for the Reynolds stresses.

APPENDIX C: REYNOLDS STRESSES TRANSPORT EQUATIONS

The Reynolds shear stress transport equations are shortly discussed here. The production, turbulent transport, pressure-velocity gradient, dissipation, and diffusion terms are denoted by $\overline{P_{u_i u_j}}$, $\overline{T_{u_i u_j}}$, $\overline{\Pi_{u_i u_j}}$, $\overline{\epsilon_{u_i u_j}}$, and $\overline{D_{u_i u_j}}$, respectively. There are terms that directly come from the presence of the traveling waves and induced by streamwise gradients of the velocity field U_i . These are discussed in the main text in detail.

The transport equation for the streamwise turbulent intensity \overline{uu} is given by

$$\frac{D\overline{uu}}{Dt} = \overline{P_{uu}} - \overline{T_{uu}} + \overline{\Pi_{uu}} - \overline{\epsilon_{uu}} + \overline{D_{uu}} = 0, \quad (\text{C1})$$

where

$$\overline{P_{uu}} = \underbrace{-2\langle uu \rangle \frac{\partial \tilde{U}}{\partial x}}_{P_{uu}^1} - \underbrace{2\langle uv \rangle \frac{\partial \tilde{U}}{\partial y}}_{P_{uu}^2} - \underbrace{2\langle uv \rangle \frac{d\tilde{U}}{dy}}_{P_{uu}^3}, \quad (\text{C1a})$$

$$\overline{T_{uu}} = \underbrace{\frac{d\langle uu \rangle \tilde{V}}{dy}}_{T_{uu}^1} + \underbrace{\frac{d\langle uv \rangle}{dy}}_{T_{uu}^2}, \quad (\text{C1b})$$

$$\overline{\Pi_{uu}} = -2 \left\langle u \frac{\partial p}{\partial x} \right\rangle, \quad (\text{C1c})$$

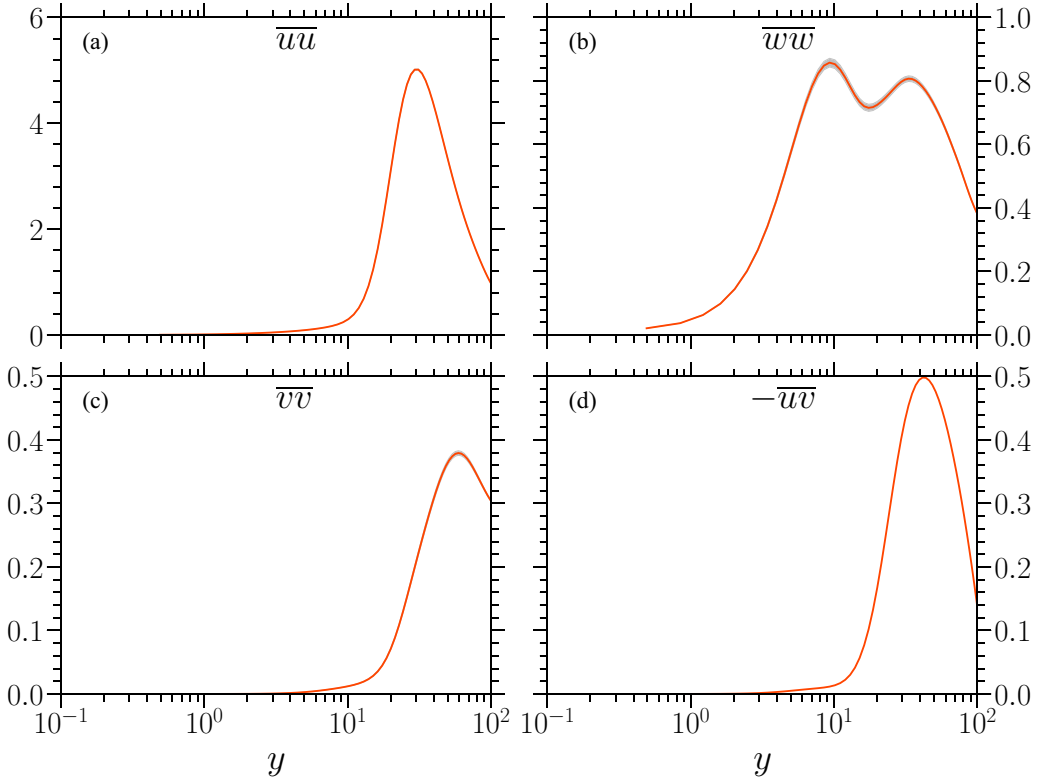


FIG. 13. Reynolds stresses profiles for the A1.25 case scaled with the local friction velocity with the corresponding error margins. (a) Streamwise component \overline{uu} , (b) spanwise component \overline{ww} , (c) wall-normal component \overline{vv} , and (d) shear stress $-\overline{uv}$.

$$\overline{\epsilon_{uu}} = 2 \left(\left\langle \frac{\partial u}{\partial x} \frac{\partial u}{\partial x} \right\rangle + \left\langle \frac{\partial u}{\partial y} \frac{\partial u}{\partial y} \right\rangle + \left\langle \frac{\partial u}{\partial z} \frac{\partial u}{\partial z} \right\rangle \right), \quad (\text{C1d})$$

and

$$\overline{D_{uu}} = \frac{d^2 \langle uu \rangle}{dy^2}. \quad (\text{C1e})$$

The transport equation for the wall normal turbulent velocity intensity \overline{vv} is given by

$$\frac{D\overline{vv}}{Dt} = \overline{P_{vv}} - \overline{T_{vv}} + \overline{\Pi_{vv}} - \overline{\epsilon_{vv}} + \overline{D_{vv}} = 0, \quad (\text{C2})$$

where

$$\overline{P_{vv}} = \underbrace{-2\langle uv \rangle \frac{\partial \tilde{V}}{\partial x}}_{P_{vv}^1} - \underbrace{2\langle vv \rangle \frac{\partial \tilde{V}}{\partial y}}_{P_{vv}^2}, \quad (\text{C2a})$$

$$\overline{T_{vv}} = \underbrace{\frac{d\langle vv \rangle \tilde{V}}{dy}}_{T_{vv}^1} + \underbrace{\frac{d\langle vvv \rangle}{dy}}_{T_{vv}^2}, \quad (\text{C2b})$$

$$\overline{\Pi_{vv}} = -2 \overline{\left\langle v \frac{\partial p}{\partial y} \right\rangle}, \quad (\text{C2c})$$

$$\overline{\epsilon_{vv}} = 2 \left(\overline{\left\langle \frac{\partial v}{\partial x} \frac{\partial v}{\partial x} \right\rangle} + \overline{\left\langle \frac{\partial v}{\partial y} \frac{\partial v}{\partial y} \right\rangle} + \overline{\left\langle \frac{\partial v}{\partial z} \frac{\partial v}{\partial z} \right\rangle} \right), \quad (\text{C2d})$$

and

$$\overline{D_{vv}} = \frac{d^2 \overline{\langle vv \rangle}}{dy^2}. \quad (\text{C2e})$$

The transport equation for the spanwise turbulent velocity \overline{ww} intensity is

$$\frac{D\overline{ww}}{Dt} = \overline{P_{ww}} - \overline{T_{ww}} + \overline{\Pi_{ww}} - \overline{\epsilon_{ww}} + \overline{D_{ww}} = 0, \quad (\text{C3})$$

where

$$\overline{P_{ww}} = \underbrace{-2 \overline{\langle wu \rangle} \frac{\partial \widetilde{W}}{\partial x}}_{\overline{P_{ww}^1}} - \underbrace{2 \overline{\langle wv \rangle} \frac{\partial \widetilde{W}}{\partial y}}_{\overline{P_{ww}^2}}, \quad (\text{C3a})$$

$$\overline{T_{ww}} = \underbrace{\frac{d \overline{\langle ww \rangle} \widetilde{V}}{dy}}_{\overline{T_{ww}^1}} + \underbrace{\frac{d \overline{\langle wwv \rangle}}{dy}}_{\overline{T_{ww}^2}}, \quad (\text{C3b})$$

$$\overline{\Pi_{ww}} = -2 \overline{\left\langle w \frac{\partial p}{\partial z} \right\rangle}, \quad (\text{C3c})$$

$$\overline{\epsilon_{ww}} = 2 \left(\overline{\left\langle \frac{\partial w}{\partial x} \frac{\partial w}{\partial x} \right\rangle} + \overline{\left\langle \frac{\partial w}{\partial y} \frac{\partial w}{\partial y} \right\rangle} + \overline{\left\langle \frac{\partial w}{\partial z} \frac{\partial w}{\partial z} \right\rangle} \right), \quad (\text{C3d})$$

and

$$\overline{D_{ww}} = \frac{d^2 \overline{\langle ww \rangle}}{dy^2}. \quad (\text{C3e})$$

Finally, the transport equation for the Reynolds shear stress $\overline{uv} < 0$ (not $-\overline{uv} > 0$) is

$$\frac{D\overline{uv}}{Dt} = \overline{P_{uv}} - \overline{T_{uv}} + \overline{\Pi_{uv}} - \overline{\epsilon_{uv}} + \overline{D_{uv}} = 0, \quad (\text{C4})$$

where

$$\overline{P_{uv}} = \underbrace{-\overline{\langle uv \rangle} \frac{\partial \widetilde{U}}{\partial x}}_{\overline{P_{uv}^1}} - \underbrace{\overline{\langle vv \rangle} \frac{\partial \widetilde{U}}{\partial y}}_{\overline{P_{uv}^2}} - \underbrace{\overline{\langle uu \rangle} \frac{\partial \widetilde{V}}{\partial x}}_{\overline{P_{uv}^3}} - \underbrace{\overline{\langle uv \rangle} \frac{\partial \widetilde{V}}{\partial y}}_{\overline{P_{uv}^4}} - \underbrace{\overline{\langle vv \rangle} \frac{d\overline{U}}{dy}}_{\overline{P_{uv}^5}}, \quad (\text{C4a})$$

$$\overline{T_{uv}} = \underbrace{\frac{d \overline{\langle uv \rangle} \widetilde{V}}{dy}}_{\overline{T_{uv}^1}} + \underbrace{\frac{d \overline{\langle uvv \rangle}}{dy}}_{\overline{T_{uv}^2}}, \quad (\text{C4b})$$

$$\overline{\Pi_{uv}} = -\overline{\left\langle u \frac{\partial p}{\partial y} \right\rangle} - \overline{\left\langle v \frac{\partial p}{\partial x} \right\rangle}, \quad (\text{C4c})$$

$$\overline{\epsilon_{uv}} = 2 \left(\overline{\left\langle \frac{\partial u}{\partial x} \frac{\partial v}{\partial x} \right\rangle} + \overline{\left\langle \frac{\partial u}{\partial y} \frac{\partial v}{\partial y} \right\rangle} + \overline{\left\langle \frac{\partial u}{\partial z} \frac{\partial v}{\partial z} \right\rangle} \right), \quad (\text{C4d})$$

and

$$\overline{D_{uv}} = \frac{d^2 \overline{uv}}{dy^2}. \quad (\text{C4e})$$

-
- [1] M. Malik, W. Liao, F. Li, and M. Choudhari, DRE-enhanced swept-wing natural laminar flow at high Reynolds numbers, in *Proceedings of the 51st AIAA Aerospace Sciences Meeting* (AIAA, Reston, VA, 2013).
 - [2] A. Rastegari and R. Akhavan, On the mechanism of turbulent drag reduction with super-hydrophobic surfaces, *J. Fluid Mech.* **773**, R4 (2015).
 - [3] M. S. Naim and M. F. Baig, Turbulent drag reduction in Taylor-Couette flows using super-hydrophobic surfaces and liquid-infused surfaces, *Phys. Fluids* **31**, 095108 (2019).
 - [4] S. Soleimani and S. Eckels, A review of drag reduction and heat transfer enhancement by riblet surfaces in closed and open channel flow, *Int. J. Thermofluids* **9**, 100053 (2021).
 - [5] P. Ricco, M. Skotes, and M. Leschziner, A review of turbulent skin-friction drag reduction by near-wall transverse forcing, *Progr. Aerospace Sci.* **123**, 100713 (2021).
 - [6] Y. Huang, L. Wang, and S. Fu, Drag reduction in turbulent channel flows by a spanwise traveling wave of wall blowing and suction, *Phys. Fluids* **33**, 095111 (2021).
 - [7] P. Olivucci, D. J. Wise, and P. Ricco, Reduction of turbulent skin-friction drag by passively rotating discs, *J. Fluid Mech.* **923**, A8 (2021).
 - [8] X. Q. Cheng, C. W. Wong, Fazle Hussain, W. Schröder, and Y. Zhou, Flat plate drag reduction using plasma-generated streamwise vortices, *J. Fluid Mech.* **918**, (A24) (2021).
 - [9] Y. Ji, J. Yao, F. Hussain, and X. Chen, Vorticity transport in turbulent channels under large-scale control via spanwise wall jet forcing, *Phys. Fluids* **33**, 095112 (2021).
 - [10] W. J. Jung, N. Mangiavacchi, and R. Akhavan, Suppression of turbulence in wall-bounded flows by high-frequency spanwise wall oscillations, *Phys. Fluids A* **4**, 1605 (1992).
 - [11] M. Quadrio, P. Ricco, and C. Viotti, Streamwise-traveling waves of spanwise wall velocity for turbulent drag reduction, *J. Fluid Mech.* **627**, 161 (2009).
 - [12] D. Gatti and M. Quadrio, Performance losses of drag-reducing spanwise forcing at moderate values of the Reynolds number, *Phys. Fluids* **25**, 125109 (2013).
 - [13] E. Hurst, Q. Yang, and Y. M. Chung, The effect of Reynolds number on turbulent drag reduction by streamwise travelling waves, *J. Fluid Mech.* **759**, 28 (2014).
 - [14] D. Gatti and M. Quadrio, Reynolds-number dependence of turbulent skin-friction drag reduction induced by spanwise forcing, *J. Fluid Mech.* **802**, 553 (2016).
 - [15] I. Marusic, D. Chandaran, A. Rouhi, M. K. Fu, D. Wine, B. Holloway, D. Chung, and A. J. Smits, An energy-efficient pathway to turbulent drag reduction, *Nature Commun.* **12**, 5805 (2021).
 - [16] F. Laadhari, L. Skandaji, and R. Morel, Turbulence reduction in a boundary layer by a local spanwise oscillating surface, *Phys. Fluids* **6**, 3218 (1994).
 - [17] K.-S. Choi, Near-wall structure of turbulent boundary layer with spanwise oscillation, *Phys. Fluids* **14**, 2530 (2002).
 - [18] G. Karniadakis and K.-S. Choi, Mechanisms on transverse motions in turbulent wall flows, *Annu. Rev. Fluid Mech.* **35**, 45 (2003).
 - [19] P. Ricco, Modification of near-wall turbulence due to spanwise oscillations, *J. Turbul.* **5**, N24 (2004).
 - [20] C. X. Xu and W. X. Huang, Transient response of Reynolds stress transport to spanwise wall oscillation in a turbulent channel flow, *Phys. Fluids* **17**, 018101 (2005).
 - [21] E. Toubert and M. A. Leschziner, Near-wall streak modification by spanwise oscillatory wall motion and drag-reduction mechanisms, *J. Fluid Mech.* **693**, 150 (2012).
 - [22] P. Ricco, C. Ottonelli, Y. Hasegawa, and M. Quadrio, Changes in turbulent dissipation in a channel flow with oscillating walls, *J. Fluid Mech.* **700**, 77 (2012).

- [23] A. Yakeno, Y. Hasegawa, and N. Kasagi, Modification of quasistreamwise vortical structure in a drag-reduced turbulent channel flow with spanwise wall oscillation, *Phys. Fluids* **26**, 085109 (2014).
- [24] L. Agostini, E. Toubert, and M. A. Leschziner, The turbulence vorticity as a window to the physics of friction-drag reduction by oscillatory wall motion, *Int. J. Heat Fluid Flow* **51**, 3 (2015).
- [25] Y. Wenjun, Z. Mengqi, C. Yongdong, and K. Boo Cheong, Phase-space dynamics of near-wall streaks in wall-bounded turbulence with spanwise oscillation, *Phys. Fluids* **31**, 125113 (2019).
- [26] A. Yakeno, Drag reduction and transient growth of a streak in a spanwise wall-oscillatory turbulent channel flow, *Phys. Fluids* **33**, 065122 (2021).
- [27] F. Auteri, A. Baron, M. Belan, G. Campanardi, and M. Quadrio, Experimental assessment of turbulent drag reduction by traveling waves in a turbulent pipe flow, *Phys. Fluids* **22**, 115103 (2010).
- [28] J. Bird, M. Santer, and J. F. Morrison, Experimental control of turbulent boundary layers with in-plane travelling waves, *Flow Turb. Comb.* **100**, 1015 (2018).
- [29] M. Quadrio and P. Ricco, The laminar generalized Stokes layer and turbulent drag reduction, *J. Fluid Mech.* **667**, 135 (2011).
- [30] M. Quadrio and P. Ricco, Critical assessment of turbulent drag reduction through spanwise wall oscillations, *J. Fluid Mech.* **521**, 251 (2004).
- [31] S. Tardu, Near wall dissipation revisited, *Int. J. Heat and Fluid Flow* **67**, 104 (2017).
- [32] S. Tardu and F. Bauer, Fine structure of the production in low to medium Reynolds number wall turbulence, *Comput. Fluids* **148**, 82 (2017).
- [33] S. Tardu, On the topology of wall turbulence in physical space, *Phys. Fluids* **29**, 020713 (2017).
- [34] O. Doche, S. Tardu, J. Schillings, and A. Capogna, Transportation and coherent structures in MHD turbulent channel flow subject to uniform streamwise and spanwise magnetic fields, *Phys. Rev. Fluids* **6**, 094605 (2021).
- [35] L. Agostini, E. Toubert, and M. A. Leschziner, Spanwise oscillatory wall motion in channel flow: Drag-reduction mechanisms inferred from DNS-predicted phasewise property variations at $Re_\tau = 1000$, *J. Fluid Mech.* **743**, 606 (2014).
- [36] A. K. M. F. Hussain and W. C. Reynolds, The mechanics of an organized wave in turbulent shear flow, *J. Fluid Mech.* **41**, 241 (1970).
- [37] T. R. Bewley, P. Moin, and R. Temam, Dns-based predictive control of turbulence: An optimal benchmark for feedback algorithms, *J. Fluid Mech.* **447**, 179 (2001).
- [38] S. Tardu, Active control of near-wall turbulence by local oscillating blowing, *J. Fluid Mech.* **439**, 217 (2001).
- [39] J. Kim, P. Moin, and R. Moser, Turbulence statistics in fully developed channel flow at low Reynolds number, *J. Fluid Mech.* **177**, 133 (1987).
- [40] S. Tardu and O. Doche, Communication between the buffer layer and the wall in a turbulent channel flow, *Int. J. Heat and Fluid Flow* **82**, 108564 (2020).
- [41] J. W. Brooke and T. J. Hanratty, Origin of turbulence producing eddies in a channel flow, *Phys. Fluids A* **5**, 1011 (1993).
- [42] See Supplemental Material at <http://link.aps.org/supplemental/10.1103/PhysRevFluids.7.054601> for λ_2 structures of A1.25 case.
- [43] X. Wu, P. Moin, J. M. Wallace, J. Skarda, A. Lozano-Durán, and J.-P. Hickey, Transitional–turbulent spots and turbulent–turbulent spots in boundary layers, *Proc. National Acad. Sci. USA* **114**, E5292 (2017).
- [44] S. Tardu, Characteristics of single and clusters of bursting events, *Exp. Fluids* **33**, 640 (2002).
- [45] R. J. Adrian, Hairpin vortex organization in wall turbulence, *Phys. Fluids* **19**, 041301 (2007).
- [46] See, <https://gricad.univ-grenoble-alpes.fr/>.
- [47] F. Bauer, S. Tardu, and O. Doche, Efficiency of high accuracy DRP schemes in direct numerical simulations of incompressible turbulent flows, *Comput. Fluids* **107**, 123 (2015).
- [48] R. D. Moser, J. Kim, and N. N. Mansour, Direct numerical simulation of turbulent channel flow up to $Re_\tau = 590$, *Phys. Fluids* **11**, 943 (1999).